Experimental diagnostics and modeling of inductive phenomena at low frequencies in impedance spectra of proton exchange membrane fuel cells

Ivan Pivac, Boris Šimić, Frano Barbir

Faculty of Electrical Engineering, Mechanical Engineering and Naval Architecture, University of Split
R. Boskovica 32, 21000 Split, Croatia

ipivac@fesb.hr, bsimic@fesb.hr, fbarbir@fesb.hr

ABSTRACT

Representation of fuel cell processes by equivalent circuit models, involving resistance and capacitance elements representing activation losses on both anode and cathode in series with resistance representing ohmic losses, cannot capture and explain the inductive loop that may show up at low frequencies in Nyquist diagram representation of the electrochemical impedance spectra. In an attempt to explain the cause of the low-frequency inductive loop and correlate it with the processes within the fuel cell electrodes, a novel equivalent circuit model of a Proton Exchange Membrane (PEM) fuel cell has been proposed and experimentally verified here in detail. The model takes into account both the anode and the cathode, and has an additional resonant loop on each side, comprising of a resistance, capacitance and inductance in parallel representing the processes within the catalyst layer. Using these additional circuit elements, more accurate and better fits to experimental impedance data in the wide frequency range at different current densities, cell temperatures, humidity of gases, air flow stoichiometries and backpressures were obtained.

Keywords:

electrochemical impedance spectroscopy, inductive phenomena, inductive loop, electrical equivalent circuit model, inertia of reactant gas

1. Introduction

Presence of inductive phenomena captured at lowest frequencies in the impedance spectra of PEM fuel cells may exhibit as an additional loop crossing on the positive side of the Im(Z) axis in the Nyquist plot, as shown in Fig. 1 (Pivac, Barbir, 2016). In literature, occurrence of inductive features at high frequencies is explained by the cables and wires of the system (i.e. parasitic feed line inductivity), which are not an integral part of the fuel cell. However, explanation of inductive phenomena at low frequencies is not so straight forward. A few inductive points or an

inductive loop as an interesting phenomenon in the EIS studies has been reported occasionally (Antoine et al., 2001; Baker et al., 2006; Bao, Bessler, 2015; Cruz-Manzo, Chen, 2013; Cruz-Manzo et al., 2016; Dale et al., 2010; Danzer, Hofer, 2009; Dhirde et al., 2010; Franco, Tembely, 2007; Holmstrom et al., 2012; Kuhn et al., 2007; Makharia et al., 2005; Mamlouk, Scott, 2011; Meyer et al., 2015; Rezaei Niya, Hoorfar, 2014; Rezaei Niya et al., 2016; Roy, Orazem, 2007; Roy et al., 2007; Schneider et al., 2008; Setzler, Fuller, 2015; Wagner, Gülzow, 2004; Wagner, Schulze, 2003; Wiezell et al., 2012; Wiezell et al., 2006a; Wiezell et al., 2006b). A review of different EIS investigations of the inductive phenomena at low frequencies (Pivac, Barbir, 2016) identified two generalized explanations as possible causes: (i) side reactions with intermediate species (Antoine et al., 2001; Baker et al., 2006; Cruz-Manzo, Chen 2013; Cruz-Manzo et al., 2016; Franco, Tembely, 2007; Kuhn et al., 2007; Makharia et al., 2005; Roy et al., 2007; Setzler, Fuller, 2015), and (ii) water transport related issues within the catalyst layer (Bao, Bessler, 2015; Holmstrom et al., 2012; Rezaei Niya, Hoorfar, 2014; Rezaei Niya et al., 2016; Schneider et al., 2008; Wiezell et al., 2012; Wiezell et al., 2006a; Wiezell et al., 2006b). In addition, it is frequently observed in the literature that the slope of the polarization curve does not match the low-frequency intercept point (at ca. 0.1–1 Hz) on the Nyquist diagram. Makharia et al. (2005) have explained the remaining inconsistency by the low-frequency inductive loop, the beginning of which can be observed in EIS experiments extended below 0.1 Hz. Chandesris et al. (2015) did not even obtained the inductive loop in their study (their measuring low-frequency limit was too high), but they have also found the difference between the slope of the polarization curve and the low-frequency resistance (in the case when the polarization curves were performed at constant air stoichiometries and diffusion effects were neglected). They have related that to oxygen variation with current in the cathode compartment, which is actually another interesting explanation of the low-frequency inductive loop given in an indirect way and it is on the trail with the explanation of the low-frequency inductive loop which will be provided in this paper. This difference can be also seen in Fig. 1, where the low-frequency resistance is marked as Total R, but it is the DC point that corresponds to the slope of the polarization curve at the current density at which the EIS was taken. However, the DC point is virtually impossible to record due to the equipment limitations, so the last measurable point (LMP) in Fig. 1 was taken at 10 mHz.
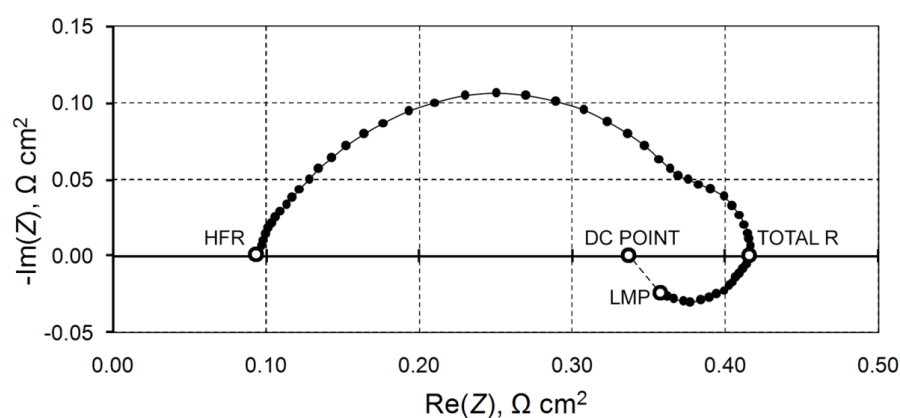
Figure 1. Typical Nyquist plot of the measured impedance data of a PEM fuel cell (50 cm^2, 65 °C, 0.5 bar(g), 15 A, H$_2$/Air stoichiometry 2/4, 100% RH) with marked intercept points: high-frequency resistance (HFR), Total R, DC point, and the last measured point (LMP)

The measured impedance spectra is often described by an equivalent circuit (EC) model of various elementary impedance elements (e.g. resistors, capacitors) as an attempt to describe the processes within the fuel cell electrochemical system, such as the electrochemical reactions, ohmic resistance and mass transfer. A standard, simple representation of the fuel cell processes by equivalent circuits involves resistance/capacitance loops (representing activation losses on both anode and cathode) in series with a resistance (representing both ionic and electrical resistance in the membrane and cell hardware) (Barbir, 2012). Very often this is simplified even further by neglecting anode's contribution (Randles equivalent circuit), or a porous bounded Warburg element or constant phase elements (CPE) are added to represent the mass transport processes at lower frequency region (capacitive loop at the right side of the Nyquist plots). However, such models cannot explain the appearance of the inductive loop at low frequencies.

Thus, proposed EIS models in the literature are of limited usefulness, and their element's explanations are often incomplete, ambiguous or insufficiently validated, and usually limited to specific operating conditions, which increases the likelihood that the physical meaning of certain elements are assigned to the wrong process due to a missing element in a model. Often, a close fit can be achieved with relatively few components, especially when constant phase elements (CPE) are used. However, the challenge is to determine which processes to include, and to associate the EC elements and their behavior back to the meaningful fuel cell processes. Since the controlling processes of the fuel cell are the slowest processes, the measured impedances at low frequencies are probably the most important part of the plot and provide very useful information, although its uncertainty is higher due to longer measuring time, because of the possible gradual system change during acquisition (Rezaei Niya, Hoorfar, 2013). Thus, the frequency range cannot be restricted to higher levels and the experimental setup needs to be modified in a way that the low frequencies can be captured in quasi-stable conditions (Rezaei Niya, Hoorfar, 2013). Also, the inductive loop must be accounted for to obtain consistent parameters when fitting a model to experimental impedance measurements and steady-state results (Setzler, Fuller, 2015). Additionally, Gomadam and Weidner (2005) have stated once: "Equivalent circuit approach normally involves oversimplified representations of the components of electrochemical systems. Therefore, this method cannot always be used to accurately describe the system and estimate parameters, especially in porous electrodes. Further, because the various transport processes occur simultaneously in porous electrodes, converting the estimated resistances and capacitances into physically meaningful parameters is difficult. The equivalent-circuit approach is good for a quick visualization tool and, perhaps, as a first approximation".

Therefore, a better understanding of inductive loop processes is still needed and current different interpretations of this phenomena have given us a new motivation to use EIS to identify other fundamental processes, which are obviously occurring within the fuel cell, but are apparently missing in diverse models from the literature. Thus, a novel EC model that is capable of capturing the processes that cause the inductive loop in the impedance spectra of PEM fuel cells at different operating conditions is proposed in this study. The model is validated

by a series of experiments varying the operating conditions (current density, temperature, humidity of reactant gases, flow rate stoichiometries, and pressure).

2. Model

In an attempt to explain the origin of the low-frequency loops and correlate this with the processes within the fuel cell, a novel 11-element impedance model of a PEM fuel cell represented by a modified equivalent circuit has been proposed and validated here. The proposed model (Fig. 2) is intrinsically a 1D description through the membrane and both electrodes. However, the model does not take into account the variation of performance across the thickness of the electrode and along the length of the flow path. The novelty is an additional loop on each side, comprising of a resistance, capacitance and inductance in parallel (so-called resonant circuit). Using these additional circuit elements, more accurate and better fits to experimental impedance data were obtained. The parameters of the model are extracted from the impedance spectra at different operating conditions in an attempt to identify the physical meaning of the each circuit element.
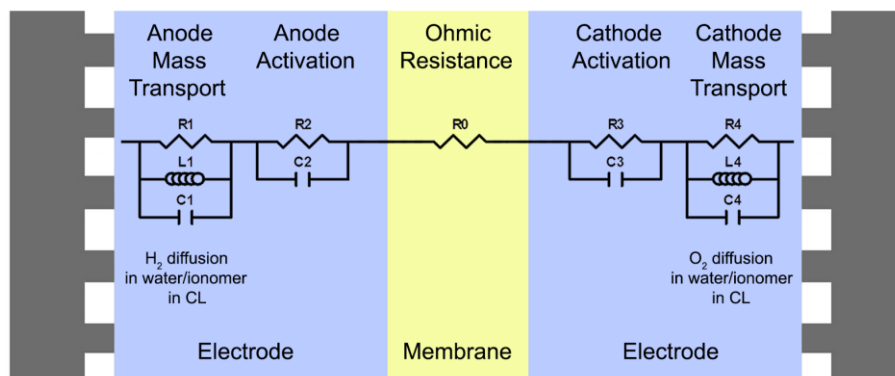
Figure 2. A novel 11-element impedance model with an approximate schematic representation of the relationship between the fuel cell geometry and the proposed electrical equivalent circuit

In this model, the physical processes preceding the catalytic reaction that take place in a complex structure of the fuel cell catalyst layer (CL) are represented by their electrical equivalents. The fuel cell electrochemical reactions take place on the catalyst surface. This surface must be accessible to all three species participating in these reactions, namely electrons, protons and reactant gases. The electrons come through the catalyst itself, and the protons come through polymer, and this polymer must contain water in order to have sufficient protonic conductivity. For this reason the active catalyst sites must be immersed in polymer. Therefore, the only way the reactant gases may be present at the catalyst/polymer interface is if they are dissolved in polymer, i.e., in water present in polymer. It is known that solubility of gases in wet polymer is higher than solubility in dry polymer and that hydrogen solubility is higher than oxygen solubility (Sakai et al., 1986; Schalenbach et al., 2015). Therefore, the

processes that precede the electrochemical reactions are conduction of electrons and protons, dissolution of reactant gases (hydrogen and oxygen) in polymer/water and diffusion of reactant gases through polymer/water to the catalyst surface. In addition, water must be present in polymer, and polymer can uptake water only to a certain limit. Water coming into the polymer or water leaving the polymer must undergo the absorption/desorption process, which has its own kinetics (Berning, 2011) and it depends on the amount and distribution of polymer in the catalyst layer as well as on the phase of water outside the polymer (i.e. liquid of vapor). Depending on conditions (temperature and pressure) and water already present in the void spaces of the catalyst layer, water may evaporate or stay in liquid form. Removal of water through the pores of the catalyst layer and then through the gas diffusion layer is much easier if water is in vapor phase.

The processes described in the preceding paragraph are much slower than conduction of protons and electrons and the electrochemical reactions, and therefore in EIS should be seen at low frequencies (Barbir, 2012; Gomadam, Weidner, 2005; O'hayre et al., 2009; Rezaei Niya, Hoorfar, 2013). In the proposed equivalent circuit model these processes are represented by inductance, resistance and capacitance connected in parallel. Mechanical equivalence of inductance is inertia. Within the catalyst layer there are two processes that may exhibit "inertia-like" behavior, namely: (i) water absorption and desorption at the polymer surface within the catalyst layer, and (ii) dissolution of reactant gases in polymer/water. Kudo et al. (2010) experimentally determined that dissolution resistance of oxygen accounts for a large part of the total oxygen transport loss. Therefore, this interphase resistance to dissolution of gas in ionomer may represent the "inertia-like" behavior. Oxygen transport inside water/ionomer is by diffusion and it should follow the Fick's law, i.e., depends on the concentration gradient. Resistance represents the resistance to transport (diffusion) of gas through water to the catalyst site (probably also the protonic resistance through ionomer within the CL), Capacitance represents stored (dissolved) quantity of gas within the water/ionomer in the CL.

The transposed parameter vector of the proposed EC model comprises of eleven parameters:

$$\theta_{EC}{}^T = [\ R_0\ \ R_1\ \ L_1\ \ C_1\ \ R_2\ \ C_2\ \ R_3\ \ C_3\ \ R_4\ \ L_4\ \ C_4\ ].$$

3. Experimental

For parameter fitting and model validation, different diagnostic techniques were performed on a single PEM fuel cell hardware from Fuel Cell Technologies with graphite four-channel serpentine cathode flow field and single-channel anode flow field, and with a 50 cm^2 active area MEA, produced by BASF (12E-W MEA). A Scribner Associates 890CL Teledyne Medusa fuel cell test station, which contains both an electronic load and a frequency response analyzer (FRA) for full range impedance measurements up to 10 kHz, was used for the experiments, especially EIS measurements which are of the relevance for the analysis presented here.

The EIS tests were performed in a current density range of 0.2–0.6 A cm^{-2}, and various operating conditions (cell temperatures, gas humidities, air flow stoichiometries and

backpressures). Reference values in all recordings were at the current density of 0.3 A cm^{-2}, cell temperature of 65 °C, with inlet relative humidities (RH) of 100% (dew point of 65 °C) for both, hydrogen on the anode, and air on the cathode. Reactants flows were set at constant stoichiometry of 2 on the anode and 4 on the cathode, while the backpressures were the same for both compartments, 0.5 bar(g).

The measurement itself was conducted in a galvanostatic mode (i.e. the current has been imposed on the cell and the voltage response was measured) in the frequency range from 3.981 kHz to 10 mHz. The frequencies were spaced in a logarithmic progression with ten points per frequency decade. Each scan took around thirty minutes and there was a five minute stabilization phase prior to each testing at the operating conditions, in order for the cell to reach the steady-state. The AC signal amplitude was selected to be 10% of the DC current to obtain a linear response from the system. In the EIS measurements in general, it is clear that the larger the AC perturbation amplitudes, the easier the separation of the measured response from noises, but also the signal amplitude has to be small enough to satisfy the linearity assumption. According to the studies conducted by Dale et al. (2010) and Chandesris et al. (2015) on the impedance spectra, which also showed that the spectrum is very scattered for low load currents (because it becomes difficult for a FRA to distinguish between the response and noise), there is no considerable difference between the impedance plots in the amplitude range of 5–10% of the DC current.

4. Results and Discussion

The proposed 11-element model was validated by a fitting procedure of the model data to the measured impedance spectrum of the cell at different current densities and various operating conditions, which is basically a least-square optimization procedure yielding the solution with the minimum sum of errors (differences between measured and calculated impedances for each of the frequencies) squared. The fit and numerical values of the model parameters for each impedance spectrum were estimated through the commercially available software ZView® 3.0 (Scribner Associates, Inc.). The software itself provides the values of the EC parameters that best fit the experimental data to the chosen model, but it needs initial values (as close as possible to the real ones) in an expected order of magnitude, in order to minimize the fitting error. The most suitable set of parameter values are the values that yield the lower χ^2 value, which is the calculated software's parameter that gives an estimation of the distance between the real data and the simulated data, i.e. the error of the fit. This parameter was used to evaluate the "goodness of fit" and it was less than 10^{-3} indicating fairly good fit, and these values with the statistical error for each estimated parameter value are included in all of the following tables in every studied case. As it can be seen in all of the Nyquist plots in figures below, a very good agreement between simulation and measured data was achieved in the whole frequency range, including the low-frequency inductive loop. Also, a good agreement between the slope of the steady-state polarization curves and the impedance extrapolated to zero perturbation frequency (DC point) was obtained. The measured data are represented in the following Nyquist diagrams as light colored lines and the simulated curves as dark colored lines.

For the first measurement (influence of current density), the model elements of membrane ohmic resistance (R0) and anode activation (R2 and C2) were held constant in this case of fitting procedure, while the other model elements were simultaneously fitted for every impedance spectra, successively for every current density from the initial one. For all other measurements, all the model elements were simultaneously fitted for every impedance spectra, successively for every studied case from the initial one.

4.1. Influence of current density on impedance spectra

In order to measure the evolution of the Nyquist impedance plots along the polarization curve (Fig. 3), the series of four EIS measurements (marked points in Fig. 3) were made from 0.2 A cm^{-2} to as high as 0.6 A cm^{-2}. In Fig. 4a, the inductive effects at low frequencies were apparent for all measured current densities in the obtained Nyquist plots, which was already reported in literature (Roy et al., 2007). The simulation results under different dc load conditions show very good agreement with those from the experimental measurement data, including the low-frequency capacitive loop followed by the inductive loop, and even exhibit non-ideal capacitive behavior (caused by the rough surface area of electrodes due to their porous structure as reported by Dhirde et al., 2010).
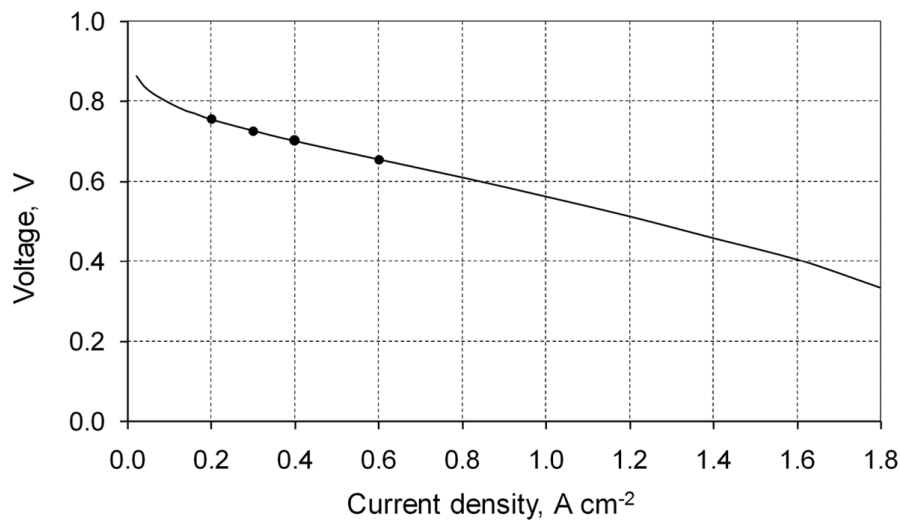

Figure 3. Polarization curve of a PEM fuel cell (50 cm^2, 65 °C, 0.5 bar(g), H_2/Air stoichiometry 2/4, 100% RH) with marked EIS measurement points
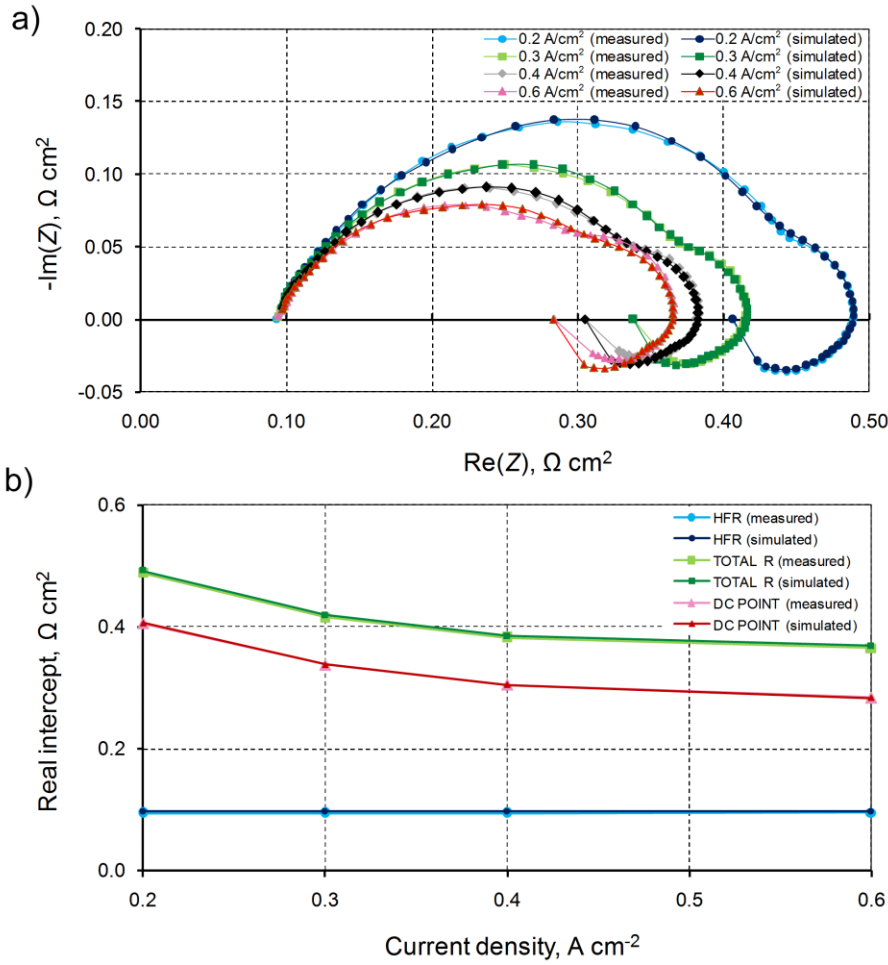
Figure 4. a) Comparison of measured and simulated impedance spectra at different operating points along the polarization curve (0.2–0.6 A cm^{-2}); b) Comparison of measured and simulated real intercept points at three characteristic frequencies as a function of current density

In Fig. 4a, each spectrum consists mainly of a small high-frequency (4–0.6 kHz) capacitive loop (HF), medium-frequency (600–8 Hz) capacitive loop (MF) and low-frequency (8–0.2 Hz) capacitive loop (LF) followed by the inductive loop at the lowest frequencies (0.2–0.01 Hz). Two overlapping loops, HF and MF, correspond to the fuel cell impedance due to anode and cathode activation processes, where the cathode impedance practically masks the impedance of the anode which indicates that the activation losses at the cathode dominate over those at the anode (Dhirde et al., 2010; O'hayre et al., 2009). Their diameters, represented by R2 and R3, reflect the effective charge transfer resistances that contribute to the anode and cathode activation losses (Dhirde et al., 2010; Malevich et al., 2008; Wagner et al., 2008). As expected, cathode charge transfer resistance turns out larger than the anode charge transfer resistance, because of slower kinetics of the oxygen reduction reaction (ORR), which increase the RC time constant of the ORR at the cathode (Dhirde et al., 2010). As HF and MF loops overlap, the effective fuel cell charge transfer resistance is assumed to be their sum. Therefore, the effective charge transfer resistance for this observed fuel cell decreased from 0.309 to 0.187 Ω cm^{-2} as current increased from 0.2 to 0.6 A cm^{-2} (Tab. 1). Comparatively, the ohmic resistance is much

lower (~0.097 Ω cm^{-2}) and constant with current density. A HF loop is always present with a small contribution regardless of any change in current density, mainly related to the hydrogen oxidation reaction (HOR) (Malevich et al., 2008), and its diameter is completely independent of the current density or gas diffusivity (Rezaei Niya et al., 2016). The measured Nyquist plots reported in literature also show that the diameter of this arc remains unchanged at different current densities (Dale et al., 2010; Danzer, Hofer, 2009; Dhirde et al., 2010; Malevich et al., 2008; Mamlouk, Scott, 2011; Rezaei Niya et al., 2016). A linear high-frequency branch of the HF is mainly associated with the processes occurring in the cathode (Holmstrom et al., 2012) and indicates ionic resistance in the catalyst layer (Makharia et al., 2005), where the straight line may be due to the porous structure of the electrode (Kuhn et al., 2007). MF reduces in size as the current density increases from 0.2 to 0.6 A cm^{-2} resembling inverse dependence of charge transfer resistance with current density (Malevich et al., 2008). LF capacitive loop moves toward real axis indicating a finite length of charge diffusion in the fuel cell and it is related to the mass transport/diffusion processes (Dhirde et al., 2010), i.e., contribution of oxygen concentration gradient in the cathode. The mass transport impedance is observed at lower frequencies because it takes time for the reactants to move and penetrate farther into the CLs and GDLs at both electrodes resulting in a higher diffusion resistance value (Dhirde et al., 2010; O'hayre et al., 2009).

Table 1. Changes of the model element values with current density

i	R0	R1	C1	L1	R2	C2	R3	C3	R4	C4	L4
[A/cm^2]	[Ωcm^2]	[Ωcm^2]	[F/cm^2]	[Hcm^2]	[Ωcm^2]	[F/cm^2]	[Ωcm^2]	[F/cm^2]	[Ωcm^2]	[F/cm^2]	[Hcm^2]
0.2	0.0964	0.0239	0.0089	0.0391	0.0827	0.0172	0.2276	0.0282	0.0609	1.1976	0.5711
	fix.	±1.49%	±1.91%	±13.75%	fix.	fix.	±0.45%	±0.66%	±2.18%	±4.87%	±4.51%
0.3	0.0964	0.0244	0.0090	0.0348	0.0827	0.0172	0.1588	0.0351	0.0562	1.0628	0.5732
	±0.20%	±4.14%	±2.38%	±12.51%	fix.	fix.	±2.48%	±5.71%	±1.93%	±4.99%	±4.22%
0.4	0.0964	0.0241	0.0092	0.0301	0.0827	0.0172	0.1256	0.0441	0.0562	0.9370	0.6083
	fix.	±1.21%	±1.51%	±8.69%	fix.	fix.	±0.57%	±0.86%	±1.52%	±3.82%	±3.24%
0.6	0.0964	0.0218	0.0096	0.0220	0.0827	0.0172	0.1036	0.0630	0.0637	0.7406	0.7107
	fix.	±1.37%	±1.92%	±10.86%	fix.	fix.	±0.87%	±1.10%	±1.56%	±3.93%	±3.44%

Parameter χ^2 was 0.001242, 0.000870, 0.000896 and 0.001207 for 0.2, 0.3, 0.4 and 0.6 A cm^{-2}, respectively.

The main results of Fig. 4a are summarized in Fig. 4b, which shows the real intercept points at three characteristic frequencies as a function of current density, and their trends are very similar and consistent with those reported in literature (Setzler, Fuller, 2015). The leftmost real-axis intercept point on the Nyquist diagram at ~4 kHz, defined as the high-frequency resistance (HFR), represents the ohmic loss in the cell and is generally taken in the frequency range 1–10 kHz due to limitations in the experimental setup and equipment (Holmstrom, 2012). This loss takes into account ionic losses in the membrane and the electrical (both electronic and contact) losses in cell hardware, but not the ionic losses within the catalyst layer. The ohmic resistance (R0 in the proposed model) or HFR value remains unchanged for all operating points (Fig. 4b and Tab. 1) because EIS measurements were performed on the cell operating with fully-hydrated reactants (i.e. water content inside the Nafion phase was constant). The impedance curve crosses the real-axis again at ~0.2 Hz in the intermediate low-frequency intercept point (the point with maximum real impedance and the highest resistive losses), defined here as the total resistance (Total R) which represents the overall loss in the cell and hence, it is modeled as the sum of all resistors in the proposed model (Total R = R0 + R1 + R2+ R3 + R4). Finally, with further decrease in frequency, the impedance curve circles back towards the real-axis to the final real-axis intercept at the zero perturbation frequency, so-called DC

point (Setzler, Fuller, 2015) or total steady-state polarization cell resistance (Wagner, 2002). Here, it was measured and calculated from the polarization curve slope at the measured EIS current density (because it is not possible to measure the impedance at infinitely low frequency) and included for comparison in the results as final filled symbol at the end of the inductive loop on the real-axis intercept. Also, it can be modeled as the difference between the total resistance (Total R) and both resonant loop resistors (DC point = Total R − R1 − R4 = R0 + R2+ R3). In order to evaluate the proposed model near DC conditions, simulations were extended to the DC point, capturing the entire inductive loop. As it can be seen in the diagrams, its values extrapolate the impedance curves perfectly and the model matches the DC steady-state resistance for all current densities.

The values of the EC model elements are extracted from the respective fitted curves and summarized in Tab. 1. As discussed above, the resistance R0 remained constant and so did, R1 and R2, resistances associated with the anode. The charge transfer resistance on the cathode (R3) dropped with current. The cathode double-layer capacitance (C3) increases (almost 2.5 times) with current density, but the cathode catalyst layer capacitance (C4) decreases (about 1.5 times) with current density, because at higher current densities oxygen is getting consumed faster than it can be dissolved and therefore its quantity in water/polymer decreases. Cathode inductance (L4) is higher than the anode's (L1), probably because oxygen, as a bigger molecule than hydrogen, is more inert to dissolve in water or ionomer in the CL. Cathode inductance increases with current as more and more oxygen must be dissolved and transported to the catalyst sites. Changes of all other parameters were either insignificant and/or probably within the error of the measurements and numerical methods involved in their calculation. The proposed impedance model appears to be able to describe the impedance spectra over the regarded current density range, and the trends of changes of the model element values are mainly consistent with the expectations based on physical interpretation.

4.2. Influence of cell operating temperature on impedance spectra

In general, a higher cell operating temperature results in higher cell potential; however, for each fuel cell design there is an optimal temperature, where the upper limit of operating temperature is determined by the membrane and its state of hydration (Barbir, 2012). For this observed cell, three different sets of experimental data were recorded at different temperatures (50, 65 and 80 °C) and the optimum operating temperature appears to be somewhere between 65 °C and 80 °C (Fig. 5a). Also, there is a clear dependence of the position of the impedance spectra along the real-axis on temperature. The size of the MF capacitive arc is the smallest at the highest temperature due to improvement of the electrochemical reactions with temperature (Wiezell et al., 2006a), but the low-frequency capacitive and inductive arcs are the smallest at the optimal temperature of 65 °C and slightly bigger at the higher temperature (Fig. 5a). Increasing the cell temperature increases hydrated Nafion phase proton conductivity, which leads to decrease in ohmic resistance (HFR in Fig. 5b and R0 in Tab. 2), but only slightly because measuring current density at 0.3 A cm^{-2} is still in predominantly activation region where the influence of the ohmic losses is low. Very similar tendency of change can also be seen at Total R and DC intercept points (Fig. 5b), but with a more expressed decrease from 50 to 65 °C, because of much more intensive reduction of MF and LF (R3 and R4, respectively, in Tab. 2).
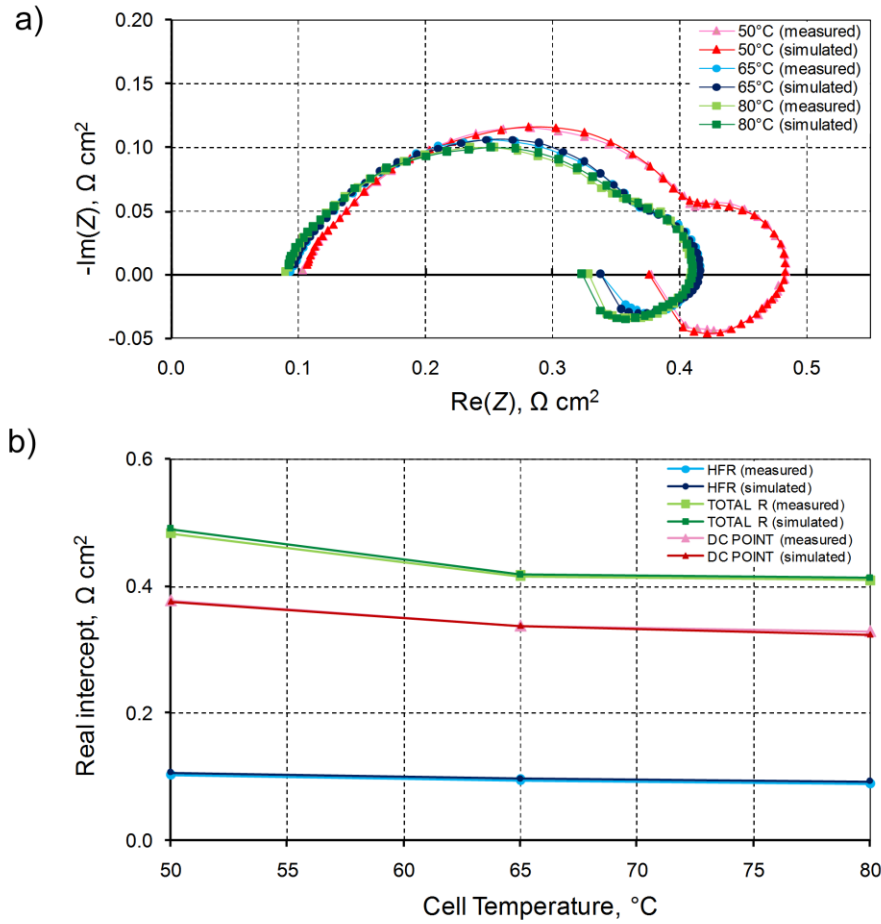
Figure 5. a) Comparison of measured and simulated impedance spectra at different cell operating temperatures (50, 65 and 80 °C); b) Comparison of measured and simulated real intercept points at three characteristic frequencies as a function of cell operating temperature

Table 2. Changes of the model element values with cell operating temperature

T_{cell}	R0	R1	C1	L1	R2	C2	R3	C3	R4	C4	L4
[°C]	[Ωcm^2]	[Ωcm^2]	[F/cm^2]	[$H cm^2$]	[Ωcm^2]	[F/cm^2]	[Ωcm^2]	[F/cm^2]	[Ωcm^2]	[F/cm^2]	[$H cm^2$]
50.0	0.1063	0.0279	0.0086	0.0368	0.0984	0.0174	0.1715	0.0410	0.0856	1.3910	0.8919
	±0.17%	±2.59%	±1.78%	±11.96%	±2.85%	±1.49%	±1.67%	±3.54%	±1.32%	±2.50%	±2.38%
65.0	0.0964	0.0244	0.0090	0.0348	0.0827	0.0172	0.1588	0.0351	0.0562	1.0628	0.5732
	±0.20%	±4.14%	±2.38%	±12.51%	±4.66%	±2.13%	±2.48%	±5.71%	±1.93%	±4.99%	±4.22%
80.0	0.0923	0.0279	0.0095	0.0357	0.0991	0.0178	0.1322	0.0546	0.0619	0.9478	0.5380
	±0.22%	±3.73%	±2.09%	±11.51%	±3.74%	±1.92%	±2.83%	±6.35%	±2.07%	±4.53%	±3.95%

Parameter χ^2 was 0.000541, 0.000870 and 0.001006 for 50, 65 and 80 °C, respectively.

Therefore, as summarized in Tab. 2, cathode charge transfer resistance (R3) decreases, and cathode double layer capacitance (C3) increases with temperature. On the other side, cathode catalyst layer resonant loop parameters (R4, L4 and C4) all decrease with temperature. The cathode inductance (L4) significantly decreased from 50 to 65 °C and after that only slightly, which can be explained by faster dissolution of oxygen in water or ionomer in the CL on the cathode side at higher temperatures, and explanation for the extremely high values for

inductance (0.5-0.9 H cm^2) can be the slowness of the reaction and huge inertia of reactant gas to be dissolved. Changes of all other parameters were either insignificant and/or probably within the error of the measurements and numerical methods involved in their calculation.

4.3. Influence of inlet relative humidity on impedance spectra

In the third EIS test series, the dew point temperatures in both humidifiers were stepwise increased from 50 °C to 59 °C to 65 °C, corresponding to 50%, 75% and 100% relative humidity at the cell operating temperature of 65 °C. Fig. 6a shows the impedance spectra at three different relative humidities. The identified impedance spectra change their shape and size only slightly, but they are horizontally shifted to the left with increasing humidity (Fig. 6a) due to decreased ohmic resistance (HFR in Fig. 6b or R0 in Tab. 3) with an increased water content in the membrane (Danzer, Hofer, 2009) (i.e. decreasing the RH of reactant gas streams increases the membrane resistance and reduces the active area (Malevich et al., 2008)).
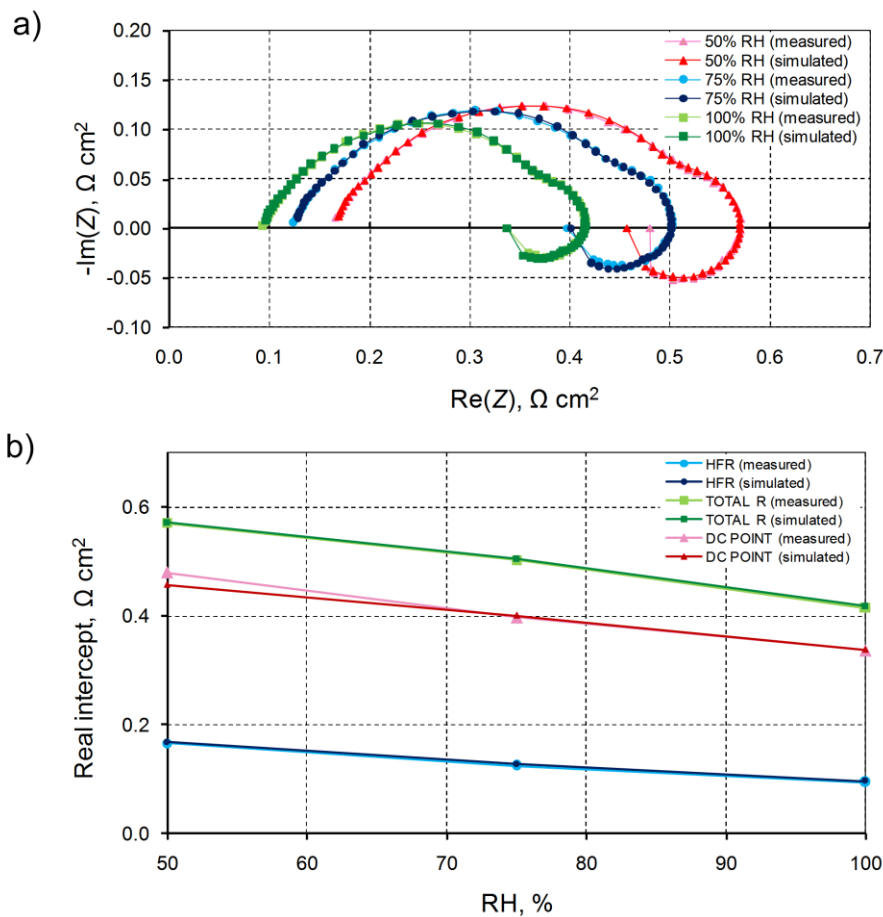

Figure 6. a) Comparison of measured and simulated impedance spectra at different inlet relative humidities (50, 75 and 100% RH); b) Comparison of measured and simulated real intercept points at three characteristic frequencies as a function of inlet relative humidity

Table 3. Changes of the model element values with inlet relative humidity

RH	R0	R1	C1	L1	R2	C2	R3	C3	R4	C4	L4
[%]	[Ωcm^2]	[Ωcm^2]	[F/cm^2]	[Hcm^2]	[Ωcm^2]	[F/cm^2]	[Ωcm^2]	[F/cm^2]	[Ωcm^2]	[F/cm^2]	[Hcm^2]
50.0	0.1678	0.0398	0.0054	0.1128	0.1279	0.0113	0.1614	0.0354	0.0745	0.7700	0.6330
	±0.16%	±2.24%	±1.79%	±5.09%	±2.28%	±1.24%	±1.83%	±3.70%	±1.37%	±3.46%	±2.68%
75.0	0.1274	0.0335	0.0072	0.0598	0.1133	0.0142	0.1603	0.0396	0.0703	0.8154	0.7203
	±0.14%	±2.42%	±1.47%	±6.49%	±2.60%	±1.30%	±1.86%	±3.92%	±1.35%	±3.04%	±2.66%
100.0	0.0964	0.0244	0.0090	0.0348	0.0827	0.0172	0.1588	0.0351	0.0562	1.0628	0.5732
	±0.20%	±4.14%	±2.38%	±12.51%	±4.66%	±2.13%	±2.48%	±5.71%	±1.93%	±4.99%	±4.22%

Parameter χ^2 was 0.000455, 0.000412 and 0.000870 for 50, 75 and 100% RH, respectively.

Very similar tendency of change can be also seen at Total R and DC intercept points (Fig. 6b), where significant drop is mainly due to already mentioned intensive decrease of ionic resistance in the membrane (HFR). MF and LF (R3 and R4, respectively, in Tab. 3) decreased only slightly with increase in relative humidity. The magnitude of the MF increases at lower humidities (Malevich et al., 2008) due to an increase in the slope of the polarization curve at lower humidities (Holmstrom et al., 2012). The transport hindrances and therewith resistances (R4 and R1 in Tab. 3) decreased with increasing humidity, especially from 75 to 100% RH, which again supports the result that the LF arc at low frequencies is dominated by transport properties (Danzer, Hofer, 2009). Rise of the inductive loop with decreasing humidity indicates that there is a slow process with a large time constant responsible for this loop and is also dependent on the humidification level in the fuel cell (Holmstrom et al., 2012), thus increase in resistance to transport (diffusion) of oxygen through water or ionomer within the CL to the catalyst site can be an explanation. Capacitance of the cathode resonant loop (C4) slightly increases with increasing humidity (Tab. 3), indicating higher water, and therefore higher oxygen content within the ionomer in the catalyst layer.

Anode side is usually more sensitive to dry conditions because of the electroosmotic drag. Therefore, parameters from the anode resonant circuit (R1, C1 and L1) definitely change with inlet relative humidity, but these values are much lower than the others and their trends of changes are insignificant from our opinion.

4.4. Influence of air flow stoichiometry on impedance spectra

In the fourth EIS test series, the air flow stoichiometry or stoichiometric ratio (S) was varied from 1.5 to 2.5 to 4.0, whilst the hydrogen flow stoichiometry was kept constant at 2.0. A large discrepancy between the obtained impedance spectra can be observed in Fig. 7a. The first intersection with the real axis (HFR in Fig. 7b) and therewith the ohmic resistance (R0 in Tab. 4) stayed unchanged for all cases. HF (R2 and C2 in Tab. 4) was barely affected by the evolution of the stoichiometry, and MF (R3 and C3 in Tab. 4) increased slightly, which seems logical since this two parts of the spectrum corresponds to charge transfer resistive and capacitive effects which does not vary a lot for a given current (Chandesris et al., 2015). However, LF increased significantly with decreasing air flow stoichiometry. These results are in accordance with the results of the preceding tests in literature, since a variation of the reactant flow stoichiometry primarily has an effect on the transport properties (Chandesris et al., 2015; Danzer and Hofer 2009). A reduced incoming mass flow of the reactants leads to a lower partial pressure at the

active surface, to a reduced concentration gradient and therewith to higher transport losses (Danzer, Hofer, 2009). Another contribution to the LF impedance can also be the result of oxygen concentration changes due to convective oxygen supply along the gas channel, without having to resort to diffusion limitations phenomena (Chandesris et al., 2015). The constant ohmic resistance implies that the fuel cell is sufficiently humidified for all stoichiometric ratios (Danzer, Hofer, 2009), which was exactly the case here (100% RH for both compartments). Also, a varied flow stoichiometry has less effect at the anode side with hydrogen (approximately negligible beyond 1.11) than at the cathode with the oxygen in the air (Danzer, Hofer, 2009). Therefore, EIS measurements with the variations of the hydrogen flow stoichiometry are not shown here.
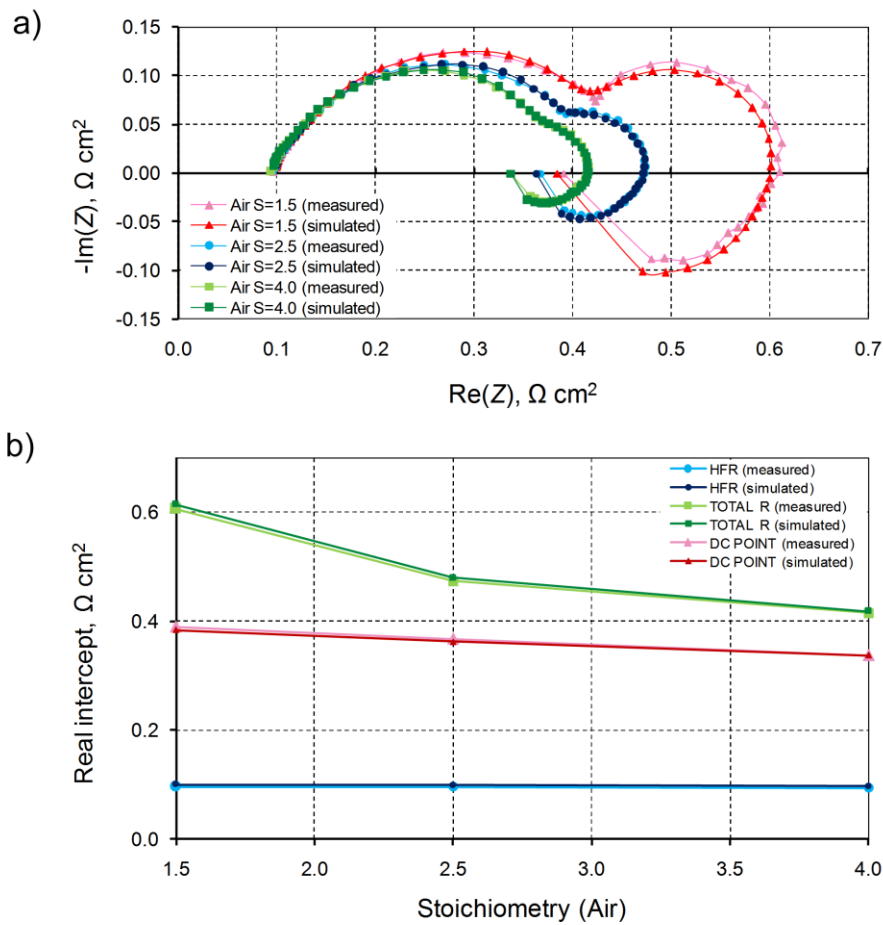

Figure 7. a) Comparison of measured and simulated impedance spectra at different air flow stoichiometries (1.5, 2.5 and 4.0); b) Comparison of measured and simulated real intercept points at three characteristic frequencies as a function of air flow stoichiometry

Table 4. Changes of the model element values with air flow stoichiometry

S_{O2}	R0	R1	C1	L1	R2	C2	R3	C3	R4	C4	L4
[ ]	[Ωcm^2]	[Ωcm^2]	[F/cm^2]	[Hcm^2]	[Ωcm^2]	[F/cm^2]	[Ωcm^2]	[F/cm^2]	[Ωcm^2]	[F/cm^2]	[Hcm^2]
1.5	0.0995	0.0317	0.0099	0.0450	0.1110	0.0198	0.1739	0.0509	0.1982	0.9040	2.7350
	±0.28%	±4.16%	±2.53%	±23.94%	±4.87%	±2.42%	±3.18%	±6.55%	±1.36%	±1.97%	±2.16%
2.5	0.0990	0.0274	0.0091	0.0306	0.1054	0.0170	0.1584	0.0483	0.0899	1.1630	0.8901
	±0.21%	±3.23%	±2.09%	±14.65%	±3.08%	±1.65%	±2.07%	±4.77%	±1.50%	±3.14%	±2.78%
4.0	0.0964	0.0244	0.0090	0.0348	0.0827	0.0172	0.1588	0.0351	0.0562	1.0628	0.5732
	±0.20%	±4.14%	±2.38%	±12.51%	±4.66%	±2.13%	±2.48%	±5.71%	±1.93%	±4.99%	±4.22%

Parameter χ^2 was 0.001268, 0.000806 and 0.000870 for 1.5, 2.5 and 4.0, respectively.

As Fig. 7b shows, both the magnitude and the characteristic points (Total R and DC point) of the inductive loop were affected by the air flow stoichiometry. The intermediate intercept of the cell spectra with the real axis at low frequencies (Total R), strongly increases as the air stoichiometry decreases. Also, the difference between the DC point obtained at constant stoichiometry and the Total R directly depends on the stoichiometry (this difference tends to zero with increasing stoichiometry in infinity), which is completely in accordance with the preceding findings in literature (Chandesris et al., 2015). Furthermore, a shift in the characteristic frequency of the Total R is also visible, which is slightly higher for a higher flow stoichiometries (around 0.14 Hz for S=1.5, 0.28 Hz for S=2.5 and 0.36 Hz for S=4.0). Similar phenomenon was already seen in the preceding tests in literature with the constant flow rates, where the top frequency of the low-frequency inductive loop was slightly higher for the higher flow rates (Holmstrom et al., 2012).

Influence of air flow stoichiometry on each EC model element is visible in their extracted values summarized in Tab. 4. R4 is the only element showing significant change (it decreases almost 4 times). This is due to increased average oxygen concentration with higher stoichiometries. At low stoichiometry (1.5), the cell experiences large mass transport loss, which is also seen in Fig. 7a as a large LF loop. Inductance (L4) decreases, and capacitance (C4) slightly increases with increased air flow rate, both indicating the effect of increased average oxygen concentration with higher stoichiometries.

4.5. Influence of operating backpressure on impedance spectra

In the fifth EIS test series, the operating backpressures for both compartments were varied from 0 to 0.5 to 1.0 bar(g) and the obtained impedance spectra are shown in Fig. 8a. Very similar trends are obtained with the previous analyses of the air flow stoichiometry effects. It can be seen that the first intersection with the real axis (HFR in Fig. 8b) and therewith the ohmic resistance (R0 in Tab. 5) stayed unchanged for all cases, HF (R2 and C2 in Tab. 5) was barely affected by the increase of the operating backpressures, but MF (R3 and C3 in Tab. 5) as well as LF increased significantly with decreasing operating backpressure. This is a direct result of the concentration of reactant gases as given by the Nernst equation (Meyer et al., 2015). Therefore, increasing the operating backpressure led to a decrease in total impedance (Total R in Fig. 8b) and DC point also (Fig. 8b).
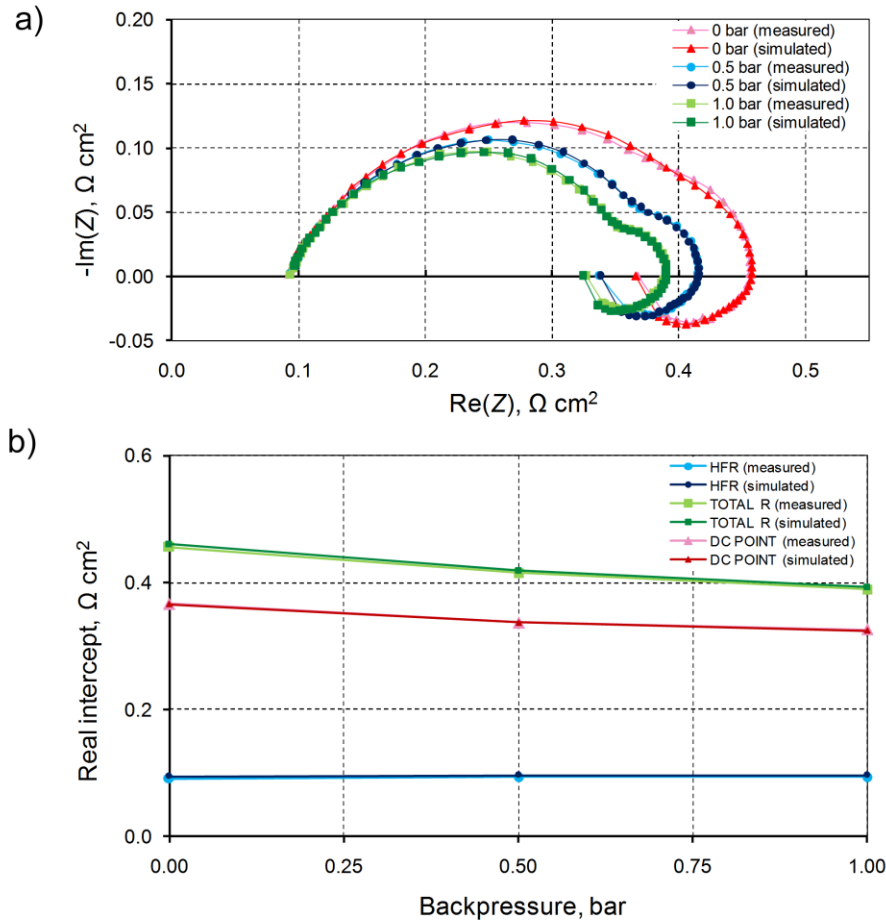
Figure 8. a) Comparison of measured and simulated impedance spectra at different operating backpressures (0, 0.5 and 1.0 bar(g)); b) Comparison of measured and simulated real intercept points at three characteristic frequencies as a function of operating backpressure

Table 5. Changes of the model element values with air flow stoichiometry

P	R0	R1	C1	L1	R2	C2	R3	C3	R4	C4	L4
[bar(g)]	[Ωcm^2]	[Ωcm^2]	[F/cm^2]	[Hcm^2]	[Ωcm^2]	[F/cm^2]	[Ωcm^2]	[F/cm^2]	[Ωcm^2]	[F/cm^2]	[Hcm^2]
0.0	0.0943	0.0268	0.0098	0.0344	0.0996	0.0199	0.1724	0.0473	0.0673	0.7424	0.6277
	±0.20%	±3.18%	±1.96%	±11.37%	±3.55%	±1.67%	±2.06%	±4.71%	±1.99%	±4.30%	±3.90%
0.5	0.0964	0.0244	0.0090	0.0348	0.0827	0.0172	0.1588	0.0351	0.0562	1.0628	0.5732
	±0.20%	±4.14%	±2.38%	±12.51%	±4.66%	±2.13%	±2.48%	±5.71%	±1.93%	±4.99%	±4.22%
1.0	0.0959	0.0219	0.0089	0.0350	0.0844	0.0152	0.1439	0.0367	0.0468	1.7664	0.4428
	±0.22%	±4.69%	±2.91%	±14.43%	±4.12%	±2.20%	±2.53%	±5.92%	±2.17%	±5.44%	±5.07%

Parameter χ^2 was 0.000855, 0.000870 and 0.001046 for 0, 0.5 and 1.0 bar, respectively.

Influence of operating backpressure on each EC model element is visible in their extracted values summarized in Tab. 5. Resistances R3 and R4 show decrease with increasing pressure due to increased oxygen concentration. Cathode catalyst layer inductance (L4) slightly decreases with pressure. Capacitance C4 increases with increased pressure much more pronounced than in the case of varying oxygen stoichiometry, which may be indicating the

effect of increased oxygen concentration, i.e., faster oxygen dissolution and higher oxygen content in ionomer in the catalyst layer.

5. Conclusions

The inductive phenomena at low frequencies in the Nyquist plots observed in PEM fuel cells have been experimentally confirmed via detailed EIS measurements at various operating conditions for the first time in this wide operating range.

A novel equivalent circuit model of a fuel cell has been proposed, with two resonant loops consisting of resistance, inductance and capacitance connected in parallel, added to the usual fuel cell representation. The two resonant loops should represent the processes inside the anode and the cathode, respectively. A series of experiments were conducted with a single fuel cell varying current density, operating temperature and pressure, relative humidity of the reactant gases, and cathode stoichiometry, and performing electrochemical impedance spectroscopy for each experiment. The model results in a very good fit to the experimental data, which allows extraction of the values of model elements and observation of the trends of their changes with operational conditions. The observed trends seem to confirm the speculated physical meanings of the added resonant loops and their elements, namely:

- Cathode catalyst layer resistance, R4, which we speculate represents resistance to oxygen supply, i.e., diffusion of oxygen inside polymer in the cathode catalyst layer, decreases with temperature, stoichiometry (i.e. oxygen concentration) and pressure. This is consistent with expectations as diffusion, actually permeation rate, increases with temperature, and concentration gradient.
- Cathode catalyst layer inductance, L4, representing inertia, i.e., interface barrier or interface dissolution rate resistance also exhibited similar behavior, i.e., decreases with temperature, stoichiometry (i.e. oxygen concentration) and pressure.
- Cathode catalyst layer capacitance, C4, which we speculate represents the quantity of stored oxygen within polymer in the catalyst layer, decreases with temperature and increases with relative humidity (i.e., water content in polymer), stoichiometry (i.e., oxygen concentration), and oxygen pressure. This is consistent with oxygen dissolution in water – it decreases with temperature, and it increases with concentration and pressure, and of course with water content.

With this equivalent circuit model it is possible to represent the observed inductive loop crossing on the positive side of the Im(Z) axis in the Nyquist plot at lowest frequencies in the impedance spectra of PEM fuel cells, which is not possible with other equivalent circuit models in the literature. As each of the elements of the proposed equivalent circuit model is related to different properties and phenomena in the cell, it is possible to quantify each of them and monitor their changes over time, and/or with changes in operating conditions. Therefore, this model can be used as a tool for condition monitoring and health assessment of PEM fuel cells, especially for lifetime and degradation tests.

Acknowledgements

References

Antoine, O., Bultel, Y., Durand R. (2001). Oxygen Reduction Reaction Kinetics and Mechanism on Platinum Nanoparticles inside Nafion®. Journal of Electroanalytical Chemistry 499(1): 85–94.

Baker, D., Gu, W., Mathias, M. F., Murphy, M. W., Neyerlin, K. C. (2006). Low-Frequency Impedance of Polymer Electrolyte Fuel Cells. Meeting Abstracts MA2005-01: 1519.

Bao, C., Bessler, W. G. (2015). Two-Dimensional Modeling of a Polymer Electrolyte Membrane Fuel Cell with Long Flow Channel. Part II. Physics-Based Electrochemical Impedance Analysis. Journal of Power Sources 278: 675–682.

Barbir, F. (2012). PEM Fuel Cells: Theory and Practice. 2nd ed. Elsevier Academic Press

Berning, T. (2011). On Water Transport in Polymer Electrolyte Membranes during the Passage of Current. International Journal of Hydrogen Energy 36(15): 9341–9344.

Chandesris, M., Robin, C., Gerard, M., Bultel Y. (2015). Investigation of the Difference between the Low Frequency Limit of the Impedance Spectrum and the Slope of the Polarization Curve. Electrochimica Acta 180: 581–590.

Cruz-Manzo, S., Chen, R. (2013). An Electrical Circuit for Performance Analysis of Polymer Electrolyte Fuel Cell Stacks Using Electrochemical Impedance Spectroscopy. Journal of the Electrochemical Society 160(10): F1109–F1115.

Cruz-Manzo, S., Perezmitre-Cruz, C., Greenwood, P., Chen, R. (2016). An Impedance Model for Analysis of EIS of Polymer Electrolyte Fuel Cells under Platinum Oxidation and Hydrogen Peroxide Formation in the Cathode. Journal of Electroanalytical Chemistry 771: 94–105.

Dale, N. V., Mann, M. D., Salehfar, H., Dhirde, A. M., Han, T.-H. (2010). Ac Impedance Study of a Proton Exchange Membrane Fuel Cell Stack Under Various Loading Conditions. Journal of Fuel Cell Science and Technology 7(3): 031010–031020.

Danzer, M. A., Hofer, E. P. (2009). Analysis of the Electrochemical Behaviour of Polymer Electrolyte Fuel Cells Using Simple Impedance Models. Journal of Power Sources 190(1): 25–33.

Dhirde, A. M., Dale, N. V., Salehfar, H., Mann, M. D., Han, T.-H. (2010). Equivalent Electric Circuit Modeling and Performance Analysis of a PEM Fuel Cell Stack Using Impedance Spectroscopy. Ieee Transactions on Energy Conversion 25(3): 778–786.

Franco, A. A., Tembely, M. (2007). Transient Multiscale Modeling of Aging Mechanisms in a PEFC Cathode. Journal of The Electrochemical Society 154(7): B712–B723.

Gomadam, P. M., Weidner, J. W. (2005). Analysis of Electrochemical Impedance Spectroscopy in Proton Exchange Membrane Fuel Cells. International Journal of Energy Research 29(12): 1133–1151.

Holmstrom, N., Wiezell, K., Lindbergh, G. (2012). Studying Low-Humidity Effects in PEFCs Using EIS I. Experimental. Journal of the Electrochemical Society 159(8): F369–F378.

Kudo, K., Suzuki, T., Morimoto, Y. (2010). Analysis of Oxygen Dissolution Rate from Gas Phase into Nafion Surface and Development of an Agglomerate Model. ECS Transactions 33(1): 1495–1502.

Kuhn, H., Wokaun, A., Scherer, G. G. (2007). Exploring Single Electrode Reactions in Polymer Electrolyte Fuel Cells. Electrochimica Acta 52(6): 2322–2327.

Makharia, R., Mathias, M. F., Baker, D. R. (2005). Measurement of Catalyst Layer Electrolyte Resistance in PEFCs Using Electrochemical Impedance Spectroscopy. Journal of The Electrochemical Society 152(5): A970–A977.

Malevich, D., Halliop, E., Peppley, B. A., Pharoah, J. G., Karan, K. (2008). Effect of Relative Humidity on Electrochemical Active Area and Impedance Response of PEM Fuel Cell. ECS Transactions 16(2): 1763–1774.

Mamlouk, M., Scott, K. (2011). Analysis of High Temperature Polymer Electrolyte Membrane Fuel Cell Electrodes Using Electrochemical Impedance Spectroscopy. Electrochimica Acta 56(16): 5493–5512.

Meyer, Q., Ronaszegi, K., Pei-June, G., Curnick, O., Ashton, S., Reisch, T., Adcock, P., Shearing, P. R., Brett, D. J. L. (2015). Optimisation of Air Cooled, Open-Cathode Fuel Cells: Current of Lowest Resistance and Electro-Thermal Performance Mapping. Journal of Power Sources 291: 261–269.

O'hayre, R., Cha, S., Colella, W., Prinz, F. B. (2009). Fuel Cell Fundamentals. 2nd ed. John Wiley & Sons

Pivac, I., Barbir, F. (2016). Inductive Phenomena at Low Frequencies in Impedance Spectra of Proton Exchange Membrane Fuel Cells - A Review. Journal of Power Sources 326: 112–119.

Rezaei Niya, M. S., Hoorfar, M. (2013). Study of Proton Exchange Membrane Fuel Cells Using Electrochemical Impedance Spectroscopy Technique - A Review. Journal of Power Sources 240: 281–293.

Rezaei Niya, M. S., Hoorfar, M. (2014). Process Modeling of the Ohmic Loss in Proton Exchange Membrane Fuel Cells. Electrochimica Acta 120: 193–203.

Rezaei Niya, M. S., Phillips, R. K., Hoorfar, M. (2016). Process Modeling of the Impedance Characteristics of Proton Exchange Membrane Fuel Cells. Electrochimica Acta 191: 594–605.

Roy, S. K., Orazem, M. E. (2007). Error Analysis of the Impedance Response of PEM Fuel Cells. Journal of The Electrochemical Society 154(8): B883–B891.

Roy, S. K., Orazem, M. E., Tribollet, B. (2007). Interpretation of Low-Frequency Inductive Loops in PEM Fuel Cells. Journal of The Electrochemical Society 154(12): B1378–B1388.

Sakai, T., Takenaka, H., Torikai, E. (1986). Gas Diffusion in the Dried and Hydrated Nafions. Journal of The Electrochemical Society 133(1): 88–92.

Schalenbach, M., Hoefner, T., Paciok, P., Carmo, M., Lueke, W., Stolten, D. (2015). Gas Permeation through Nafion. Part 1: Measurements. Journal of Physical Chemistry C 119(45): 25145–25155.

Schneider, I. A., Bayer, M. H., Wokaun, A., Scherer, G. G. (2008). Impedance Response of the Proton Exchange Membrane in Polymer Electrolyte Fuel Cells. Journal of The Electrochemical Society 155(8): B783–B792.

Setzler, B. P., Fuller, T. F. (2015). A Physics-Based Impedance Model of Proton Exchange Membrane Fuel Cells Exhibiting Low-Frequency Inductive Loops. Journal of the Electrochemical Society 162(6): F519–F530.

Wagner, N. (2002). Characterization of Membrane Electrode Assemblies in Polymer Electrolyte Fuel Cells Using A.c. Impedance Spectroscopy. Journal of Applied Electrochemistry 32(2002): 859–863.

Wagner, N., Gülzow, E. (2004). Change of Electrochemical Impedance Spectra (EIS) with Time during CO-Poisoning of the Pt-Anode in a Membrane Fuel Cell. Journal of Power Sources 127(1–2): 341–347.

Wagner, N., Kaz, T., Friedrich, K. A. (2008). Investigation of Electrode Composition of Polymer Fuel Cells by Electrochemical Impedance Spectroscopy. Electrochimica Acta 53(25): 7475–7482.

Wagner, N., Schulze, M. (2003). Change of Electrochemical Impedance Spectra during CO Poisoning of the Pt and Pt-Ru Anodes in a Membrane Fuel Cell (PEFC). Electrochimica Acta 48(25–26): 3899–3907.

Wiezell, K., Holmstrom, N., Lindbergh, G. (2012). Studying Low-Humidity Effects in PEFCs Using EIS II. Modeling. Journal of the Electrochemical Society 159(8): F379–F392.

Wiezell, K., Gode, P., Lindbergh, G. (2006a). Steady-State and EIS Investigations of Hydrogen Electrodes and Membranes in Polymer Electrolyte Fuel Cells: I. Modeling. Journal of The Electrochemical Society 153(4): A749–A758.

Wiezell, K., Gode, P., Lindbergh, G. (2006b). Steady-State and EIS Investigations of Hydrogen Electrodes and Membranes in Polymer Electrolyte Fuel Cells: II. Experimental. Journal of The Electrochemical Society 153(4): A759–A764.